AIAA JOURNAL
Vol. 33, No. 5, May 1995

Turbulence Modeling of Confined Flow in Rotating Disk Systems

L. Elena* and R. Schiestel†
Institut de Mécanique des Fluides, Marseille 13003, France

Turbulent confined flows with strong rotation are a severe test for turbulence models. The present work considers more specifically the numerical prediction of the turbulent flow in rotor–stator systems with and without throughflow. The turbulent flow regimes are treated on the basis of one-point closures with three different turbulence models: a k–ε low Reynolds number model, a zonal modeling using an algebraic stress model linked to the k–ε model near the walls, and a full Reynolds stress transport closure. The computational procedure is based on a finite volume method and has been validated on experimental data. A study of the influence of the rotation rate on the flow is done. Even if discrepancies remain, the second-order models including low Reynolds number treatment provide better predictions than the low Reynolds number k–ε model and prove to be a suitable level of closure necessary to deal with such complex situations.

Nomenclature

a	= disk inner radius
b	= disk outer radius
Cw	= dimensionless mass flow rate, $Q/\nu b$
$c_1, c_2, c_1', c_2', c_s, c_z, c_{\varepsilon 1}, c_{\varepsilon 2}, c_{\varepsilon 3}, c_\mu$	= modeling constants
e	= inlet radius
G	= gap ratio, s/b
k	= turbulent kinetic energy
k_{me}	= maximum value of k in the Ekman layers
k_{mi}	= maximum value of k in the inlet region
n_i	= unit vector normal to the wall
P	= mean pressure
p	= fluctuating pressure
r	= radius
Re	= rotational Reynolds number, $\Omega b^2/\nu$
Re_t	= turbulence Reynolds number, $k^2/\nu\tilde{\varepsilon}$
R_{ij}	= Reynolds stress tensor
s	= axial width of the cavity
U_i	= mean absolute velocity
U_r, U_θ, U_z	= radial, tangential, and axial components of the mean velocity in an absolute frame of reference
V_e	= average inflow velocity
V_i	= mean relative velocity
V_r, V_θ, V_z	= radial, tangential, and axial components of the mean velocity in the rotating frame
v_i	= fluctuating velocity
z	= axial coordinate
ε	= dissipation rate of turbulent kinetic energy
ε_{ij}	= dissipation rate of Reynolds stress tensor
ε_{ijk}	= orientation tensor
θ	= circumferential coordinate
ν	= kinematic viscosity
ν_t	= turbulent viscosity
ρ	= density
$\sigma_{(k)}$	= generalized Prandtl number for k
$\sigma_{(\varepsilon)}$	= generalized Prandtl number for ε
τ	= wall shear stress
ψ	= streamfunction
Ω	= angular speed
ω_i	= components of the rotation vector $(\Omega, 0, 0)$
$(1, 2, 3)$	= tensor indices (z, r, θ)

Received Jan. 21, 1994; revision received July 11, 1994; accepted for publication Aug. 17, 1994.

*Doctoral Researcher, Centre National de la Recherche Scientifique, IM2, Unité Mixte 34, 1, rue Honnorat.

†Research Scientist, Centre National de la Recherche Scientifique, IM2, Unité Mixte 34, 1, rue Honnorat.

I. Introduction

THE present study is concerned with the numerical prediction of the turbulent flow inside rotor–stator systems with and without throughflow. This kind of flow is particularly important for the turbomachinery industry. Indeed, in order to improve the performance of the jet aircrafts, the engineers must have accurate knowledge of the flow structure in the different parts of the engine. Moreover, because of severe temperature and rotation conditions, the experiments in the domain of turbomachinery are difficult and expensive and a detailed description of the flow can not be obtained. Thus, a numerical approach is a valuable tool in order to predict the heat and mass transfer and the flow structure. In this paper, we propose a study of idealized rotor–stator systems. These simple geometries allow us to describe the main phenomena which occur in this type of flow and to compare the performances of different turbulence models with experimental data.

One of the first studies of the flow in rotor–stator systems was done by Daily and Nece.[1] Their attention was focused on the experimental and theoretical studies of the different regimes which can exist in a closed cavity. They have shown that the structure of the flow in rotor–stator systems depends on both the rotation Reynolds number and the gap ratio $G = s/b$ and showed the existence of four regimes: two laminar and two turbulent regimes, each of which corresponds either to merged boundary layers or separated boundary layers. A few years later, Daily et al.[2] carried out a study including the effects of an imposed throughflow. They put forward the importance of the inlet flow passage geometry on development of the Ekman layer and on the velocity of the rotating core. More recently, Itoh et al.[3] made an experimental study of the turbulent flow inside an enclosed disk. They performed measurements of the mean velocity and of all of the components of Reynolds stress. They found that the flow is more turbulent in the stator boundary layer than in the rotor side as well as the possible existence of a laminar region (near the rotation axis), even for high rotation rates.

Because of numerical and turbulence modeling difficulties, the first numerical studies of the flow inside rotor–stator systems appeared only recently. In 1987, Morse[4] used a modified version of the low Reynolds number k–ε model proposed by Launder and Sharma.[15] This model gave encouraging results, but it had the tendency to predict an unrealistically large laminarized region. Chew and Vaughan,[5] using a finite difference procedure, computed solutions of Reynolds equations in a rotor–stator system using a mixing length model. Their results, compared to the experimental data of Daily and Nece[1] and Daily et al.,[2] were satisfactory, although there were some discrepancies in the core region. Iacovides and Theofanopoulos[6] adopted a zonal turbulence modeling approach;

a k–ε model or an algebraic stress modeling was used in the fully turbulent region of the flow, whereas for the wall treatment different mixing length hypotheses were employed. They found that none of the near-wall models examined appeared to be entirely satisfactory. They suggested that the use of an anisotropic model may become necessary for the prediction of such complex cases. Wilson et al.[7] used a multigrid code which embodies a low Reynolds number k–ε model and obtained mean velocity profiles in quite good agreement with experimental data. In a recent study by Iacovides and Toumpanakis,[8] four turbulence models were tested; a k–ε model coupled with a one-equation model, a k–ε model of Launder and Sharma,[15] a k–ω model, and a low Reynolds number differential stress model. They showed that the addition of the Yap[9] length scale correction term improved all of the predictions. They also successfully introduced an empirical modification of the ε equation in order to take into account the effect of the solid body rotation on the dissipation rate of turbulence.

The preceding brief review was limited to turbulence modeling and numerical contributions. Numerous experimental, theoretical, or numerical works involving rotating disk systems have been done in the past. A comprehensive review has been given in Refs. 10 and 11.

II. Physical and Mathematical Models

A. Geometrical Configurations

The rotor–stator systems considered here are axisymmetric with rectangular cross section. One of the configurations studied is the enclosed rotating disk. Itoh et al.[3] made a detailed experimental study of this type of flow. They not only give mean flow measurements but also a complete set of Reynolds stress components. Daily et al.[2] conducted measurements of the mean flow in a rotor–stator system with an axial inflow. This flow is useful when studying the influence of an injected throughflow. We propose here to compare our results to the experimental data in order to test the capabilities of the different levels of turbulence closure, and also to do a numerical study of the effect of rotation and injection on the structure of the flow up to $Re = 10^7$.

The geometries of rotor–stator systems are sketched in Fig. 1 and their dimensions are given in Table 1.

B. Mathematical Model

1. Mean Flow Equations

For an incompressible fluid, the governing continuity and momentum equations of the mean flow are derived from the Navier–Stokes equations using the Reynolds decomposition and statistical averaging. They can be formulated in a rotating frame of reference, as follows:

$$\frac{dV_i}{dt} = -\left(\frac{P}{\rho}\right)_{,i} + \left(\frac{\Omega^2 r^2}{2}\right)_{,i} - 2\varepsilon_{ipq}\omega_p V_q + (\nu V_{i,j} - R_{ij})_{,j}$$
$$V_{i,i} = 0 \tag{1}$$

where R_{ij} denotes the Reynolds stress tensor components. In the particular case of Cartesian coordinates, the operator $(\ )_{,i}$ is equal to the usual partial derivative $\partial/\partial x_i$. But in the case considered here of cylindrical coordinates, we note that $V_{i,j} = \partial V_i/\partial x_j$ except for $V_{r,\theta} = (1/r)(\partial V_r/\partial\theta) - V_\theta/r$ and $V_{\theta,\theta} = (1/r)(\partial V_\theta/\partial\theta) + V_r/r$. In the same way, $P_{,j} = \partial P/\partial x_j$ except for $P_{,\theta} = (1/r)(\partial P/\partial\theta)$ and analogous relations for the Reynolds stresses derivation. Tensorial notation has been kept in the following in order to preserve the generality.

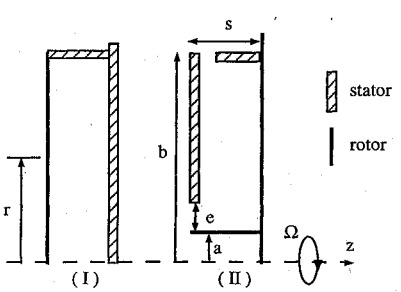

Fig. 1 Geometries studied: closed rotor–stator system, geometry I, and rotor–stator system with throughflow, geometry II.

Table 1 Size of the rotor–stator systems under consideration

Cavity type	a/s	b/s
I	0	12.5
II	1.6	14.5

Table 2 Numerical constants of the k–ε model

$c_{\varepsilon 1}$	$c_{\varepsilon 2}$	c_μ	$\sigma_{(k)}$	$\sigma_{(\varepsilon)}$
1.44	1.92	0.09	1.0	1.21

To close the system (1), we have used three types of turbulence models: a low Reynolds number k–ε model, a zonal approach with an algebraic stress model (ASM) in the core region linked to the previous low Reynolds number k–ε model in the near-wall region, and a full Reynolds stress transport closure (RSM) applicable down to the wall including the viscous sublayer.

Numerous versions of a one-point closure are derived from the energy-dissipation scheme (k–ε model) and from the stress transport models (see Refs. 12 and 13). We choose here the standard form of these models which has been largely used in the past and can be considered as a reference point. More sophisticated forms will be considered in future work.

2. k–ε Low Reynolds Number Model

The basic form of the low Reynolds number k–ε model was first introduced by Jones and Launder.[14] We retained here Launder and Sharma's version.[15] In fact, this model has already been used extensively for the study of a large range of flows and is generally considered as a good compromise between accuracy and universality for practical applications.[12] The turbulent stresses are obtained from the classical gradient law

$$R_{ij} = \tfrac{2}{3}k\delta_{ij} - \nu_t(V_{i,j} + V_{j,i}) \tag{2}$$

The turbulence viscosity ν_t is given as a function of the turbulent kinetic energy and its dissipation rate ε

$$\nu_t = c_\mu f_\mu (k^2/\tilde{\varepsilon})$$

with

$$f_\mu = \exp\left[\frac{-3.4}{(1 + Re_t/50)^2}\right]$$

In a classic way, the turbulent diffusion of k and ε are modeled using a generalized turbulent Prandtl number. The transport equations then read (the constants are given in Table 2)

$$\frac{dk}{dt} = \nu_t(V_{i,j} + V_{j,i})V_{i,j} + \left[\left(\nu + \frac{\nu_t}{\sigma_{(k)}}\right)k_{,i}\right]_{,i} - \left(\tilde{\varepsilon} + 2(\sqrt{k}_{,i})^2\right) \tag{3}$$

$$\frac{d\tilde{\varepsilon}}{dt} = C_{\varepsilon 1}\nu_t\frac{\tilde{\varepsilon}}{k}(V_{i,j} + V_{j,i})V_{i,j} - C_{\varepsilon 2}f_\varepsilon\frac{\tilde{\varepsilon}^2}{k} + \left[\left(\nu + \frac{\nu_t}{\sigma_{(\varepsilon)}}\right)\tilde{\varepsilon}_{,i}\right]_{,i} + 2\nu\nu_t V_{i,jk}V_{i,jk} \tag{4}$$

where

$$\tilde{\varepsilon} = \varepsilon - 2\nu(\sqrt{k}_{,i})^2, \qquad f_\varepsilon = 1 - 0.22\exp\left(-Re_t^2/36\right)$$

and

$$Re_t = k^2/\nu\tilde{\varepsilon}$$

3. Second-Moment Closures

The transport equations for the turbulent Reynolds stresses written in a rotating frame of reference read

$$\frac{\partial R_{ij}}{\partial t} + C_{ij} = P_{ij} + \Omega_{ij} + \Phi_{ij} - \varepsilon_{ij} + D_{ij} \tag{5}$$

with the advection term

$$C_{ij} = V_k R_{ij,k}$$

the production term

$$P_{ij} = -R_{ik}V_{j,k} - R_{jk}V_{i,k}$$

the explicit effect of rotation

$$\Omega_{ij} = -2\varepsilon_{jpq}\omega_p R_{qi} - 2\varepsilon_{ipq}\omega_p R_{qj}$$

the pressure-strain correlation

$$\Phi_{ij} = \overline{(p/\rho)(v_{i,j} + v_{j,i})}$$

the viscous dissipation rate

$$\varepsilon_{ij} = 2\nu\overline{v_{i,k}v_{j,k}}$$

and the turbulent and molecular diffusions

$$D_{ij} = [\overline{v_i v_j v_k} - \overline{(p/\rho)(v_i\delta_{jk} + v_j\delta_{ik})} + \nu R_{ij,k}]_{,k}$$

The three last terms require modeling. The main closure hypotheses rely on the standard Launder et al.[16] model. The pressure-strain correlation is split in three parts

$$\Phi_{ij} = \Phi_{ij}^{(1)} + \Phi_{ij}^{(2)} + \Phi_{ij}^{(w)}$$

including the nonlinear contribution, the linear term, and wall proximity effect, respectively. The noteworthy closure hypotheses are shortly recalled; the first term is modeled by the classical Rotta's return to isotropy approximation

$$\Phi_{ij}^{(1)} = -c_1(\varepsilon/k)\left(R_{ij} - \tfrac{2}{3}k\delta_{ij}\right)$$

The second term, which represents the linear return to isotropy, is given by

$$\Phi_{ij}^{(2)} = -c_2\left(\tilde{P}_{ij} - \tfrac{2}{3}P\delta_{ij}\right)$$

with

$$\tilde{P}_{ij} = P_{ij} + \tfrac{1}{2}\Omega_{ij}$$

and

$$P = \tfrac{1}{2}\tilde{P}_{ii} = \tfrac{1}{2}P_{ii}$$

This term embodies an implicit effect of rotation coming from the pressure interactions.[17] Other formulations have been introduced,[18] but the present choice is the natural one when applying the ASM model. The last term groups the wall effect on the Reynolds stresses and is given by[19]

$$\Phi_{ij}^{(w)} = \sum_{l=r,z}\left[c_1'\frac{\varepsilon}{k}\left(R_{km}n_k n_m\delta_{ij} - \tfrac{3}{2}R_{ki}n_k n_j - \tfrac{3}{2}R_{kj}n_i n_k\right)\right.$$

$$\left. + c_2'\left(\Phi_{km}^{(2)}n_k n_m\delta_{ij} - \tfrac{3}{2}\Phi_{ik}^{(2)}n_k n_j - \tfrac{3}{2}\Phi_{kj}^{(2)}n_i n_k\right)\right]\frac{k^{\frac{3}{2}}}{c_z\varepsilon y_1}$$

with y_1 being the distance to the wall.

In the case of the Reynolds stress transport model, we have used the formulation introduced by Hanjalic and Launder[20] in order to take into account the nonisotropic dissipation near the wall

$$\varepsilon_{ij} = -\tfrac{2}{3}\left[(1 - f_s)\delta_{ij} + \left(R_{ij}/\tfrac{2}{3}k\right)f_s\right]$$

with

$$f_s = \frac{1}{1 + Re_t^*/10}$$

and

$$Re_t^* = k^2/\nu\varepsilon$$

In the case of the algebraic stress model only a high Reynolds number version is used in the core of the flow; thus, according to the local isotropy of turbulence, the dissipation term is given by

$$\varepsilon_{ij} = \tfrac{2}{3}\varepsilon\delta_{ij}$$

For the diffusion term, we have retained the simplified formulation of Daly and Harlow[21] which was used in Refs. 16 and 20

$$-\overline{v_i v_j v_k} = c_s(k/\varepsilon)R_{k1}R_{ij,l}$$

The values of the constants are given in Table 3. The dissipation rate is obtained using its modeled transport equation

$$\frac{\mathrm{d}\varepsilon}{\mathrm{d}t} = -C_{\varepsilon 1}(\varepsilon/k)R_{ij}V_{i,j} - C_{\varepsilon 2}f_\varepsilon(\varepsilon\tilde{\varepsilon}/k)$$

$$+ (C_\varepsilon(k/\varepsilon)R_{ij}\varepsilon_{,j} + \nu\varepsilon_{,i})_{,i} + C_{\varepsilon 3}\nu(\varepsilon/k)R_{jk}V_{i,jl}V_{i,jl} \tag{6}$$

$$f_\varepsilon = 1 - \frac{0.4}{1.8}\exp\left[-(Re_t^*/6)^2\right]$$

Table 3 Modeling numerical constants

c_1	c_2	c_S	c_1'	c_2'	c_Z	c_ε	$c_{\varepsilon 1}$	$c_{\varepsilon 2}$	$c_{\varepsilon 3}$
1.8	0.6	0.22	0.5	0.3	2.5	0.15	12.75	1.8	2

4. Algebraic Stress Model

To derive the algebraic relation, we have adapted the Rodi's hypothesis for rotating flows in order to deal with objective tensors[17] only

$$\left.\begin{aligned} C_{ij} - \tfrac{1}{2}\Omega_{ij} &= C(R_{ij}/k) \\ D_{ij} &= D(R_{ij}/k) \end{aligned}\right| \quad \begin{cases} C = \tfrac{1}{2}C_{jj} \\ D = \tfrac{1}{2}D_{jj} \\ P = \tfrac{1}{2}P_{jj} \end{cases}$$

and by replacing the terms in Eq. (5), we obtain the following relation:

$$\frac{R_{ij} - \frac{2}{3}k\delta_{ij}}{k} = \frac{1 - c_2}{r_1}\frac{\tilde{P}_{ij} - \frac{2}{3}P\delta_{ij}}{\varepsilon} + \frac{\Phi_{ij}^{(w)}}{r_1\varepsilon} \tag{7}$$

with

$$r_1 = c_1 + (P/\varepsilon) - 1$$

For the ASM model, the kinetic turbulent energy k and its dissipation rate ε are obtained with Eqs. (2) and (3), replacing the turbulent diffusivity by a tensorial diffusion $k\,R_{ij}/\tilde{\varepsilon}$.

The present ASM model is not able to treat the low turbulent Reynolds number flows. Thus, to compute the flow near the wall, this model is linked to the k–ε model of Launder and Sharma.[15] The change of model is switched at a normalized distance to the wall of 0.07. The determination of the matching location between the ASM model used in the core and the low Reynolds number k–ε model used in the wall layer is known to be somehow tricky. The location needs to be far enough away from the solid surface so that the near-wall viscous effects are small and, hence, the high Reynolds number ASM is applicable. At the same time, it should be close enough to the wall so that the strong anisotropy in the turbulent normal stresses can be captured by the ASM and the discontinuity in the stress components at the matching point be minimal. The use of a single global matching distance for all four walls is a compromise. The choice of some local value of y^+ would have been, perhaps, more physical but would have led to intricate complexities in the numerics. Our choice has been to include the main part of

the Ekman layer into the low Reynolds number k–ε zone. Doing so, the results are not very sensitive to the precise location of change of model. Indeed, we have lost a part of information on the anisotropy in Reynolds stress near the wall, but if lower values of normal distance are used, the result can be more sensible to the location of change in the model.

C. Computational Aspects

1. Finite Volume Discretization

The code used is an outgrowth of the TEAM code (UMIST, Manchester). It is a finite volume code using staggered grids to solve the system of partial differential equations. We have adapted the initial two-dimensional code to deal with rotating flows. Thus, tangential components, Coriolis, and centifugal terms were introduced. The code is able to treat the equations in a rotating frame or in an absolute one; the results are obviously frame independent.

The convection and diffusion terms are discretized with the power-law scheme.[22] The velocity-pressure coupling is solved using the SIMPLER algorithm,[22] which proved to be more robust than SIMPLE for strong rotation rates. The discretized transport equations are successively solved by the Thomas algorithm.

High-rotation rates lead to severe stability problems; to overcome them, several stabilizing techniques were introduced in the code. Thus, an implicit treatment of the Coriolis terms[17] was developed and used with success. In the case of the second-order ASM closure, the code uses the stabilization practices introduced by Huang and Leschziner[23] which include a fourth grid for discretization of the shear stresses. We have also used a direct method to solve the 6×6 systems for the Reynolds stress components, which was necessary to reach the convergence of the algorithm. Because of all of these stabilizing practices, the convergence of the algorithm was obtained for cases with strong rotation. In the case of stress transport modeling, all of the stress components are solved at the same grid nodes, and the system is solved by the point block implicit method.

A study of the grid independence of the solution was done, and thus we have chosen a 80×100 point grid for geometry I and 100×200 for geometry II. The size of the near-wall cells is very reduced. The meshes are built according to geometrical series variations going from a wall cells defined by $\Delta z = 2 \times 10^{-4}$, $\Delta r = 3 \times 10^{-4}$ to the central core region cell characterized by $\Delta z = 2 \times 10^{-2}$, $\Delta r = 1.5 \times 10^{-1}$.

2. Boundary Conditions

The studied cavities present four types of boundary conditions: wall, inlet, outlet, and symmetry axis. At a rotating wall, the circumferential velocity component is set equal to Ωr and zero on the stator, like all of the other variables in a fixed frame. At the inlet, the profiles of all quantities are imposed, including a given low turbulence level $k/V_e^2 = 10^{-3}$. This value does not have a real influence on the flow within the cavity. In fact, the turbulence level calculated inside the cavity is always greater than 10^{-3}. The shear stresses are assumed to vanish at the symmetry line and the gradients of all of the other variables are zero. At the outlet, the radial velocity is calculated using the continuity equation whereas the pressure is kept constant. In order to examine a possible mainstream gas ingress, a free boundary is used for all of the other variables. It can be written as: if $V_r \geq 0$ then $d\phi/dr = 0$, if $V_r \leq 0$ then $\phi = \phi_{ext}$, where ϕ_{ext} is the given external value of ϕ.

III. Results for the Enclosed Rotating Disk

A. Structure of the Flow

According to the study of Owen and Rogers,[11] this cavity has a gap ratio large enough to present separated boundary layers. Thus, the fluid moves outward along the rotating disk and returns radially inward along the stator, such that the motion of the fluid is concentrated along the walls of the cavity and a central core is formed where the radial and axial velocities are nearly zero. The calculations were carried out for the rotational Reynolds numbers 2.5×10^5, 5.625×10^5, and 10^6. Only this last case was treated with the ASM and RSM models. Our numerical results are compared to the experimental data of Itoh et al.[3]

B. Velocity Profiles

The profiles of circumferential velocity obtained with the three models are shown in Fig. 2 and compared with experimental data for a Reynolds number of 10^6. They show, as does the experiment, a large flat core region where the velocities are nearly constant corresponding to a geostrophic flow. For the different radii, the levels of U_θ are somehow different. Itoh et al.[3] explain this difference by a change of regime. Indeed, at $r/b = 0.4$ the flow is still laminar, because of the relatively low local Reynolds number ($Re_l = \Omega r^2/\nu = 1.6 \times 10^5$), and fully turbulent at $r/b = 0.8$. The velocity level in this region is in satisfactory agreement with the measurements.

Figure 3 shows comparisons between experimental data and the calculated radial profiles using the three turbulence closures for

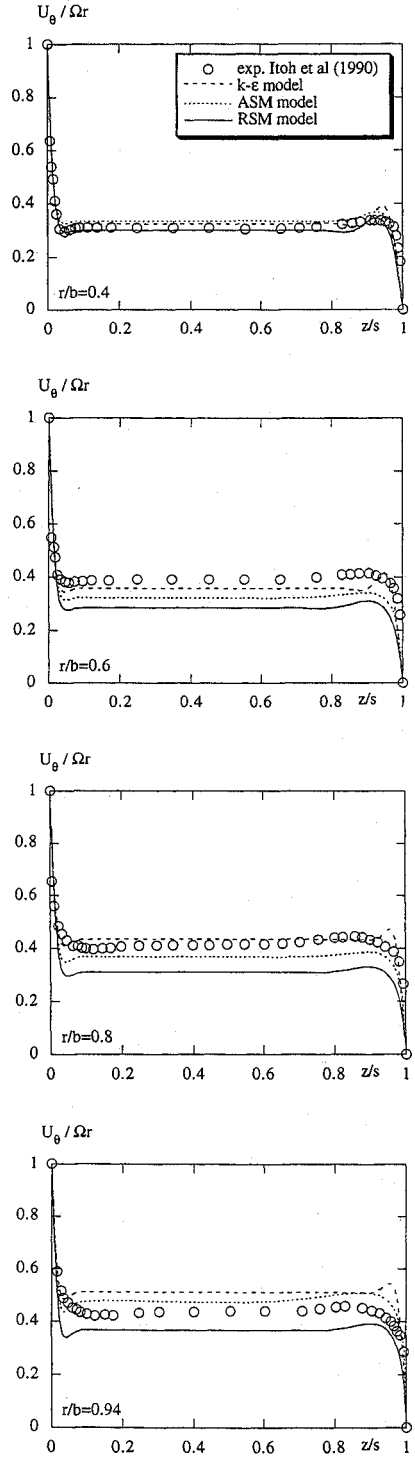

Fig. 2 Tangential velocity profiles for different radii, $Re = 10^6$, geometry I.

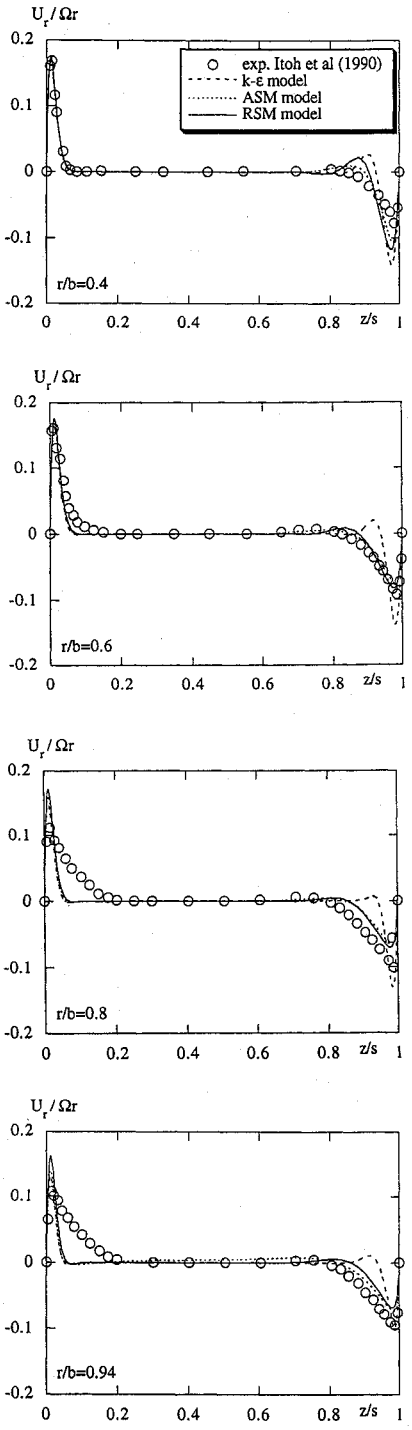

Fig. 3 Radial velocity profiles for different radii, $Re = 10^6$, geometry I.

different radii. On the rotor side, the predictions underestimate the Ekman boundary-layer thickness and the discrepancy increases at large radii. This is probably because the numerical models give almost a laminar result near the rotor. Morse[4] also found that the Launder and Sharma k–ε model[15] produce an excessive laminarization near the disks. On the stator side, the same behavior is produced by the k–ε model whereas the ASM and RSM models provide a clear improvement. Indeed, Itoh et al.[3] have shown that the flow is more turbulent near the stator than near the rotor. This can explain the fact that the models behave differently near the two lateral walls.

These remarks are confirmed by the polar profiles in the hodograph plane (Fig. 4) which describe the behavior of the three-dimensional boundary layers on the disks. Indeed, near the rotor, the calculated polar profiles fall very near the laminar profile given by an analytical solution.[24] On the stator side, the calculated polar

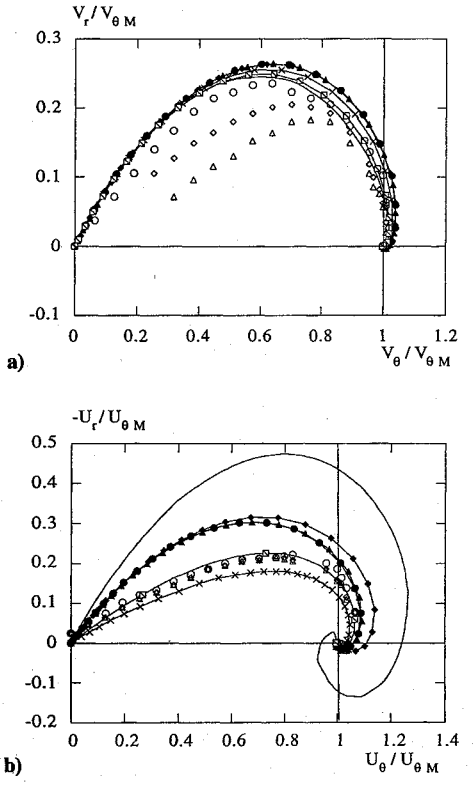

Fig. 4 Hodograph, $r/b = 0.8$, — laminar profile, ○ experiment $Re = 2.5 \times 10^5$, ◇ experiment $Re = 5.625 \times 10^5$, △ experiment $Re = 10^6$, —◆— k–ε model, $Re = 2.5 \times 10^5$, —▲— k–ε model, $Re = 5.625 \times 10^5$, —●— k–ε model, $Re = 10^6$, —×— ASM model, $Re = 10^6$, —▧— RSM model, $Re = 10^6$, geometry I: a) rotor side, normalized by $V_{\theta M}$, circumferential velocity at midline and b) stator side, normalized by $U_{\theta M}$, circumferential velocity at midline.

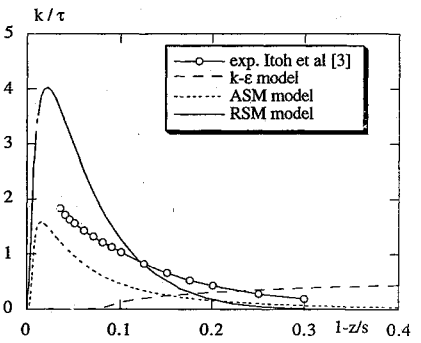

Fig. 5 Turbulent kinetic energy profile on stator side, $r/b = 0.8$, geometry I.

profiles are very different from the laminar solution, the ASM and RSM models being in good agreement with measurements.

C. Turbulent Field

Figure 5 shows the numerical and experimental turbulent kinetic energy profiles. The k–ε model which gives a quasilaminar solution totally fails to mimic the energy distribution. The two second-moment closures provide the right behavior, with a maximum in the Ekman layer, but the levels are still poorly predicted. Comparisons of the Reynolds stress components are seen in Fig. 6. For the ASM model, the levels of the Reynolds stresses near the stator side are globally well predicted. As expected, satisfactory results are obtained in the core region but not near the wall, since the k–ε model does not permit the computation of accurate Reynolds stresses. The behavior of the RSM model is particularly interesting to note. Indeed, the two components of the Reynolds stress tensor parallel to the wall are well predicted, whereas the fluctuations normal to the wall are highly overestimated (this explains the abnormally high value of the turbulent energy). The shape of

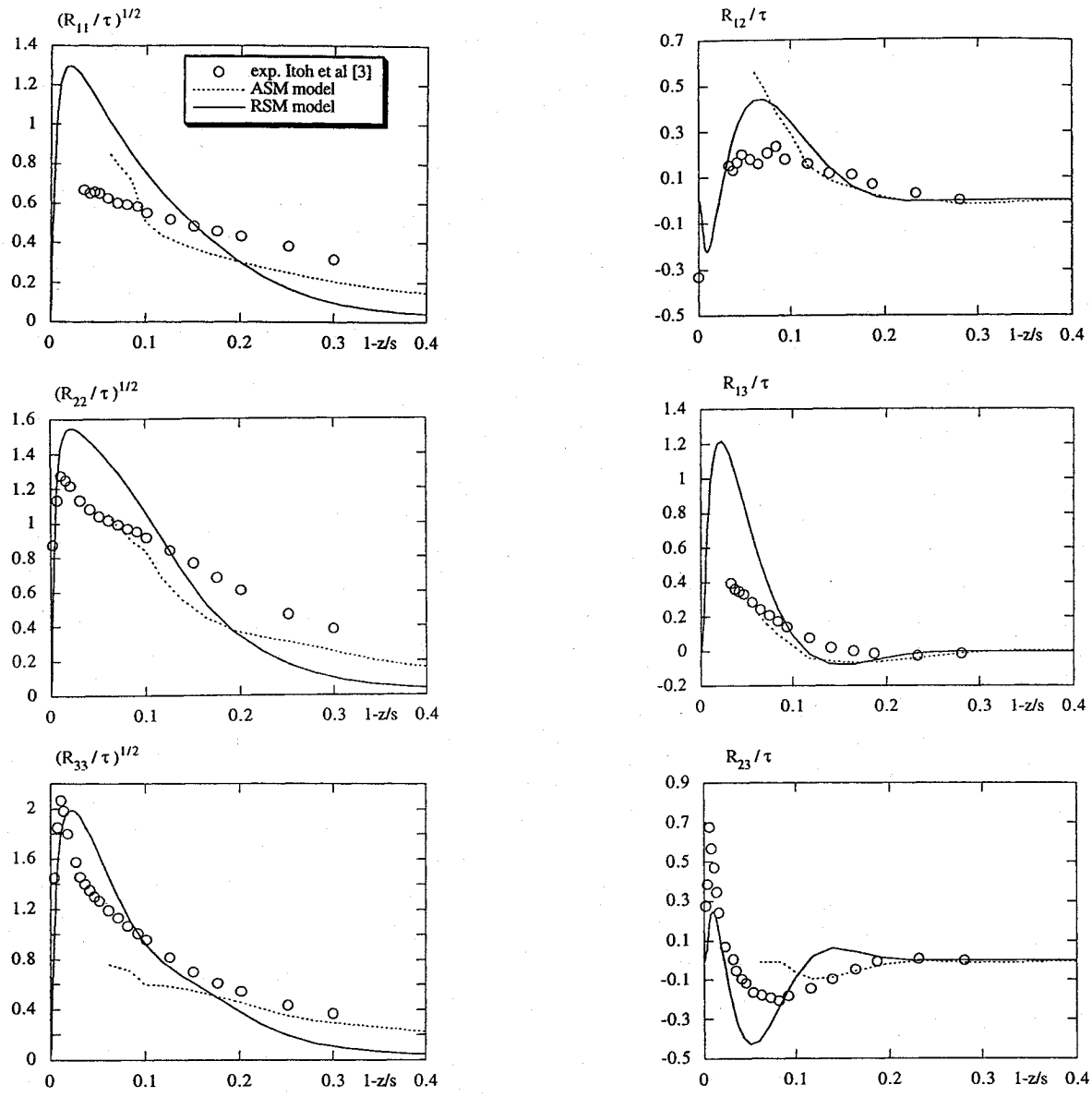

Fig. 6 Normal and shear Reynolds stresses on stator side, r/b = 0.8, geometry I.

the variation of the shear stress near the wall is correct, however, the amplitude of variation is overestimated. To improve the prediction of the relative levels of individual Reynolds stress components, a more refined modeling is probably necessary to take into account the indirect and subtle effects of rotation on the turbulent field itself.

IV. Results for the Rotor–Stator System with Throughflow

A. Structure of the Flow

In the case of a rotor–stator system with throughflow, the structure of the flow is more complex than in a closed cavity (Fig. 7). The flow can be split in four main regions: a source region in the inner part of the cavity, with a recirculating bubble due to the axial inflow; Ekman layers along the lateral walls; a Stewartson layer near the external shroud; and a recirculating bubble in the outer part of the cavity which is regulated by rotation. The variety of these structures, where the effect of the rotation and of the imposed throughflow compete, reinforces how instructional the study of this cavity is. The computations were carried on with the k–ε model for a dimensionless mass flow rate equal to 3795 and for Reynolds numbers ranging between 10^5 and 10^7. This latter case corresponds to a rotation rate of about 30,000 rpm. We present also the results obtained with the RSM model in the case of $Re = 6.9 \times 10^5$ and $Cw = 3795$. The experimental data are from Daily et al.[2]

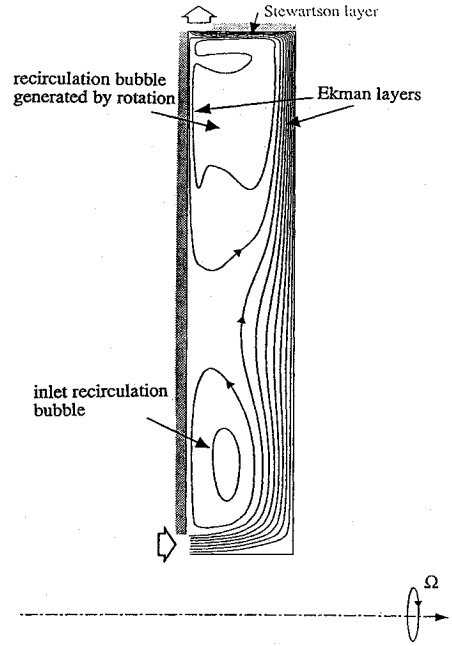

Fig. 7 Structure of the flow, geometry II.

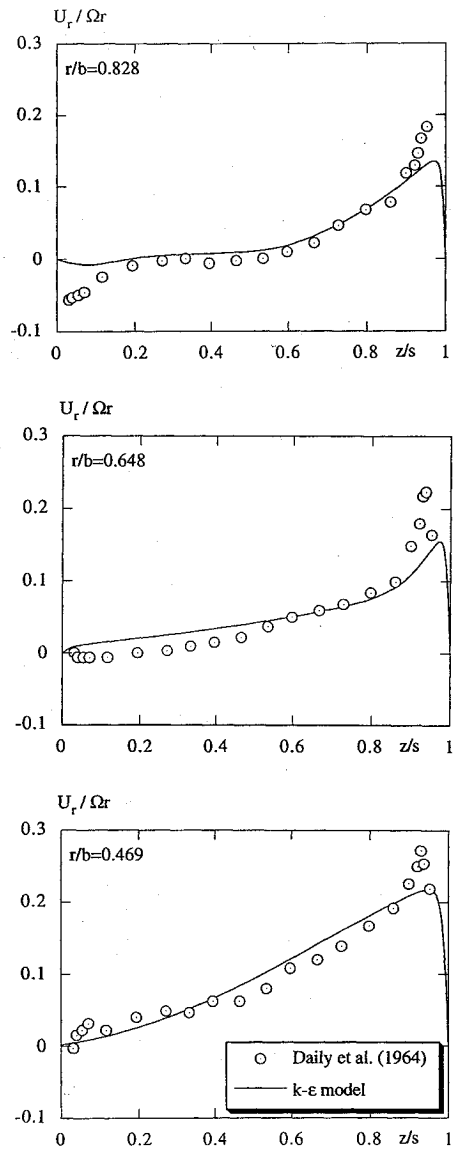

Fig. 8 Radial velocity profiles for different radii, $Re = 2.9 \times 10^5$, geometry II.

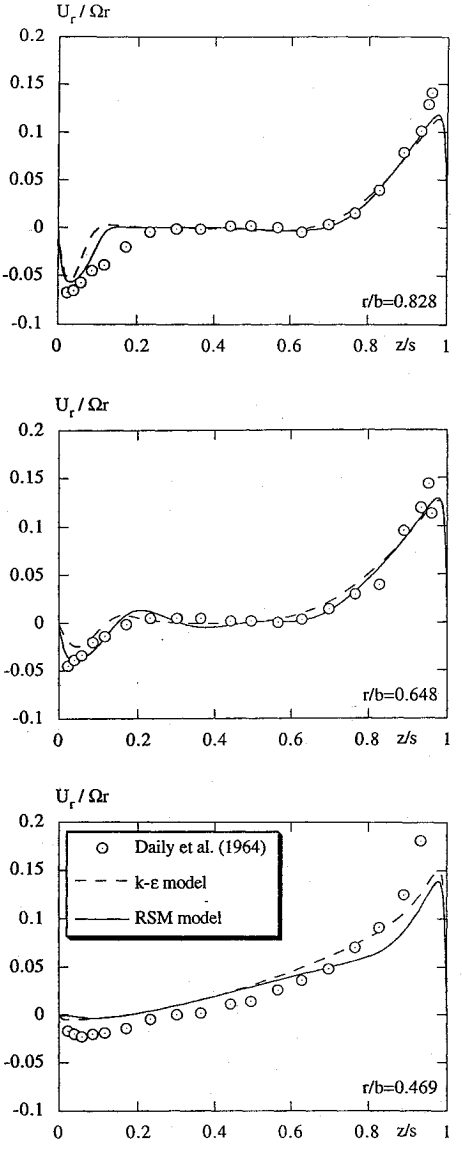

Fig. 9 Radial velocity profiles for different radii, $Re = 6.9 \times 10^5$, geometry II.

B. Velocity Profiles

To validate the code for a study of the influence of the rotation on the structure of the flow, we have carried out comparisons with experimental data. Figures 8 and 9 show the radial velocity profiles for the rotation Reynolds numbers $Re = 2.9 \times 10^5$ and 6.9×10^5. For the lower rotation rate, most parts of the cavity are dominated by the imposed throughflow and there is no Ekman layer except in the very outer part of the cavity where a zero radial velocity central region appears. For $Re = 6.9 \times 10^5$, Ekman layers are present in the half-outer part of the cavity, and the central core is distinctly defined. In both cases, the numerical results are in good agreement with the experimental data. The results obtained with the RSM model show a slight improvement for the prediction of the Ekman layers.

Comparisons of the tangential velocity are made in Fig. 10 for a Reynolds number of 6.9×10^5. The k–ε model leads to an underestimate of the rotational speed of the fluid in the core region. In fact, this is a radial shift of profiles, the calculated levels being close to the experimental ones at lower radii. This fact may be explained by small discrepancies in the inlet region that propagate at outer positions. Indeed, Daily et al.[2] have shown the strong influence of the inlet conditions on the rotation rate of the central core. This remark seems to be confirmed by the RSM model which gives similar rotation rate. In spite of this discrepancy, the numerical predictions seem to be accurate enough to make a more extensive physical study of the flow structures.

C. Influence of the Rotation on the Flow

We have plotted the tangential (Fig. 11) and radial (Fig. 12) velocity profiles at different Reynolds numbers. The tangential velocity distributions describe the progressive entrainment of the fluid inside the cavity. For $Re \leq 2.9 \times 10^5$, the tangential velocity is very low except in the vicinity of the rotor. This behavior is probably due to the strong imposed inflow (the inflow tangential velocity being zero). The profiles for $Re = 6.9 \times 10^5$ and 10^6 show a relative maximum near the stator, which is found to be characteristic of a laminar flow (confirmed by the analytical profile of laminar Ekman layers[24]). As the rotation rate increases, this maximum vanishes and normalized value $U_\theta / \Omega r$ in the core of the flow tends to the value 0.4. These two phenomena are representative of a turbulent flow in closed rotor–stator systems.[3] Figure 12 illustrates the corresponding development of the Ekman layers on radial profiles inside the cavity. At lower rotation rate, the radial velocity varies almost linearly deep in the core of the cavity. As the rotation increases, the Ekman layers develop on both disks and show a central region where the radial velocity vanishes.

The streamlines and circumferential isovelocities are given in Figs. 13 and 14 for Reynolds numbers between 10^5 and 10^7. For the weak rotation case, the flow exhibits a recirculation bubble due to the axial inflow, represented by a linear streamlines pattern. Under the effect of rotation, Ekman layers develop on both lateral walls and a recirculating bubble appears in the outer part of the cavity. As the rotation increases, this bubble and the Ekman layers

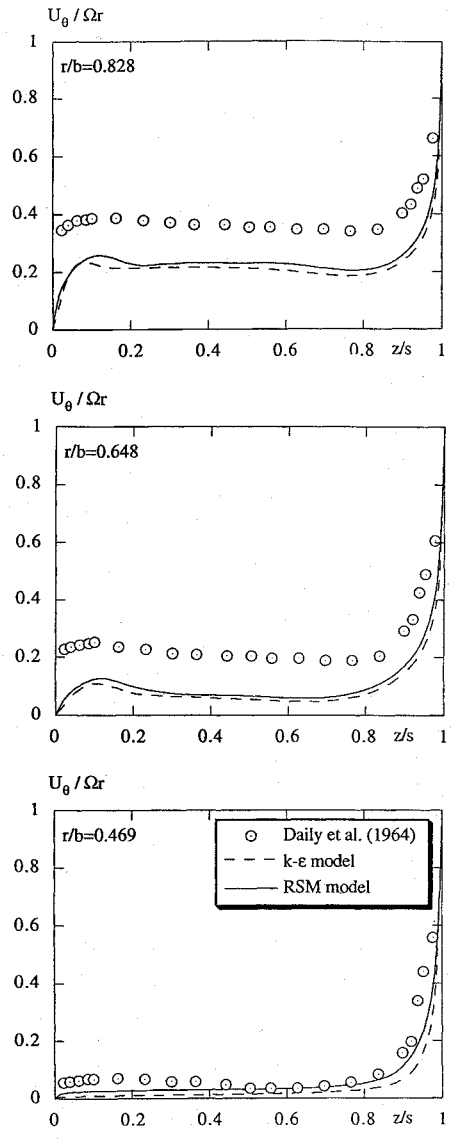

Fig. 10 Tangential velocity profiles for different radii, $Re = 6.9 \times 10^5$, geometry II.

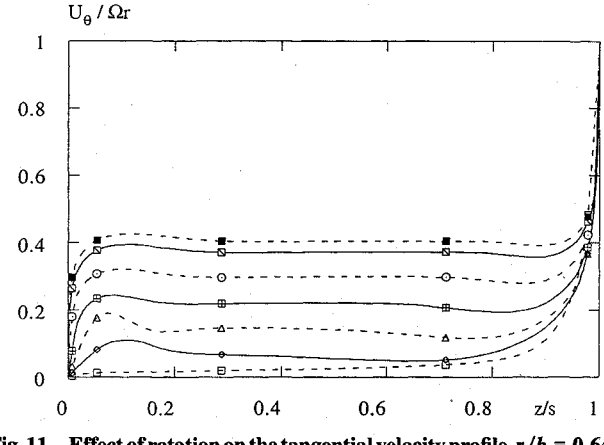

Fig. 11 Effect of rotation on the tangential velocity profile, $r/b = 0.648$, geometry II: $Re = 2.9 \times 10^5$, $Re = 6.9 \times 10^5$, $Re = 10^6$, $Re = 1.5 \times 10^6$, $Re = 2.5 \times 10^6$, $Re = 5 \times 10^6$, $Re = 10^7$.

develop simultaneously and extend over the upper-half of the cavity for $Re = 10^6$. For the higher rotation rates the structure of the outer recirculating bubble is very similar to the one found in a closed rotor–stator system. The bean-shaped streamline is characteristic of a flow inside a rotor–stator system with nonrotating shroud.[11] The circumferential isovelocities show the progressive entrainment of the fluid inside the cavity. It should be noted that the size of the

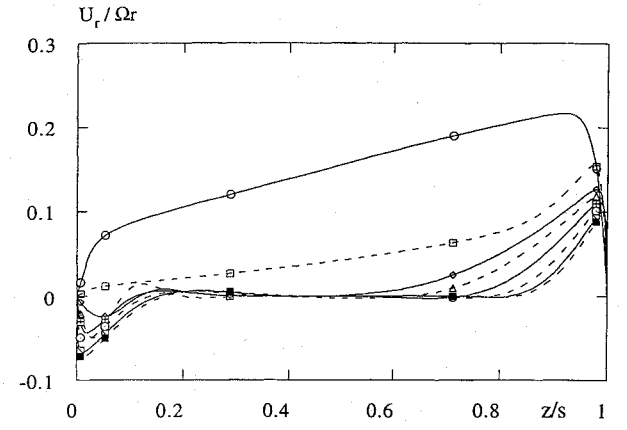

Fig. 12 Effect of rotation on the radial velocity profile, $r/b = 0.648$, geometry II: $Re = 10^5$, $Re = 2.9 \times 10^5$, $Re = 6.9 \times 10^5$, $Re = 10^6$, $Re = 1.5 \times 10^6$, $Re = 2.5 \times 10^6$, $Re = 5 \times 10^6$, $Re = 10^7$.

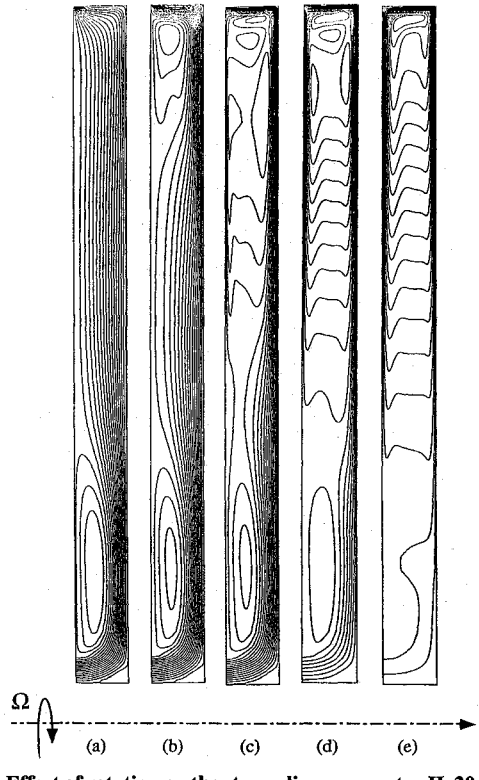

Fig. 13 Effect of rotation on the streamlines, geometry II, 20 regularly spaced intervals: a) $Re = 10^5$, $0 \leq \psi/V_e a \leq 1.65$, b) $Re = 2.9 \times 10^5$, $0 \leq \psi/V_e a \leq 1.71$, c) $Re = 10^6$, $0 \leq \psi/V_e a \leq 1.94$, d) $Re = 2.5 \times 10^6$, $0 \leq \psi/V_e a \leq 4.09$, and e) $Re = 10^7$, $0 \leq \psi/V_e a \leq 16.44$.

recirculating bubble corresponds with the part of fluid which has a circumferential velocity $U_\theta/\Omega r \geq 0.05$.

For the cavity under consideration, two sources of turbulence exist, on one hand the axial inflow impingement against the wall and on the other hand the shear in the Ekman layers. The isovalues of kinetic energy of turbulence are given in Fig. 15. For $Re = 10^5$, there is no Ekman layer and the kinetic turbulent energy is concentrated in the inner region. As the rotation increases, the turbulence develops progressively, first along the rotor and, then, downward along the stator. The case $Re = 10^6$ belongs to the transitional regime in which the effect of the inflow balances the effect of the rotation. The maximum values of the kinetic turbulent energy in the inner region and in the Ekman layers are given in Table 4 which displays the respective influence of the two sources of turbulence. For $Re \leq 5 \times 10^6$, we can note that the turbulence level in the inlet region normalized by the average inflow velocity is independent of the rotation, that means that k_{mi} only depends on the imposed throughflow. For the two higher rotation rates, the Ekman layers extend down to the

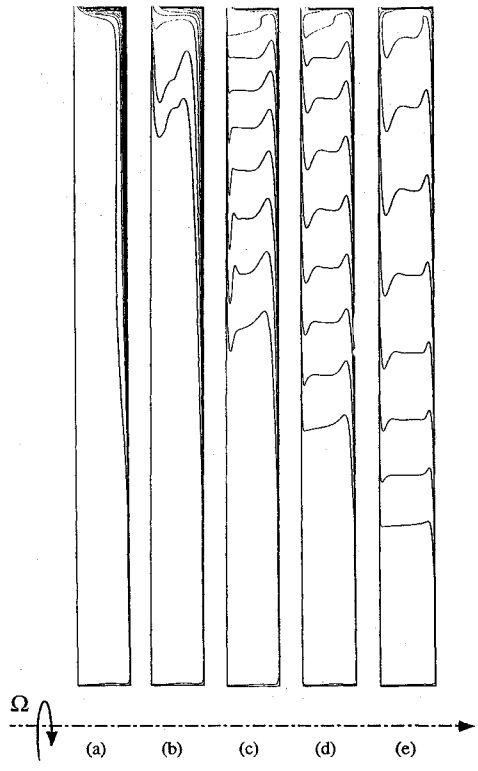

Fig. 14 Effect of rotation on the tangential velocity, geometry II, 20 regularly spaced intervals, $0 \leq U_\theta/\Omega r \leq 1$: a) $Re = 10^5$, b) $Re = 2.9 \times 10^5$, c) $Re = 10^6$, d) $Re = 2.5 \times 10^6$, and e) $Re = 10^7$.

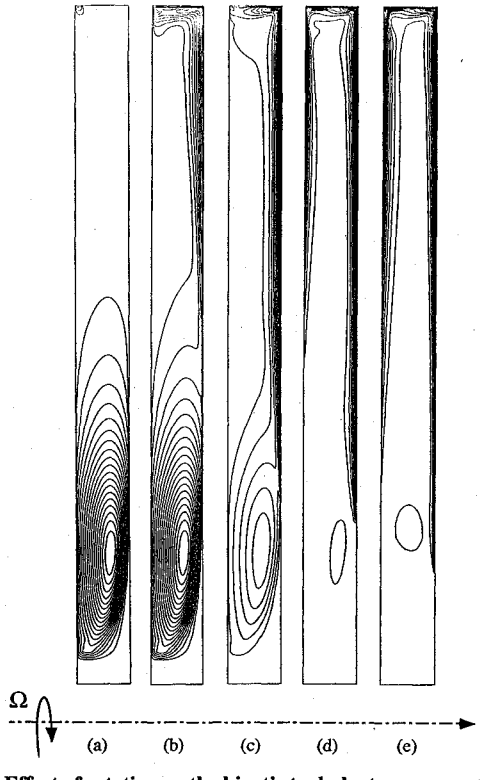

Fig. 15 Effect of rotation on the kinetic turbulent energy, geometry II, 20 regularly spaced intervals: a) $Re = 10^5$, $0 \leq k/V_e^2 \leq 0.082$, b) $Re = 2.9 \times 10^5$, $0 \leq k/V_e^2 \leq 0.082$, c) $Re = 10^6$, $0 \leq k/V_e^2 \leq 0.28$, d) $Re = 2.5 \times 10^6$, $0 \leq k/V_e^2 \leq 1.45$, and e) $Re = 10^7$, $0 \leq k/V_e^2 \leq 17.1$.

axis, which involves an increase of the turbulence level. Inversely, the maximum of kinetic turbulent energy inside the Ekman layers normalized by the rotation speed, first increases with the rotation then reaches a constant value of about 5×10^{-3} as soon as the outer recirculating bubble occupies more than half of the cavity.

Table 4 Maxima of the kinetic energy of turbulence for geometry II

Re	k_{me}/V_e^2	k_{mi}/V_e^2	$k_{me}/\Omega^2 b^2$	$k_{mi}/\Omega^2 b^2$
10^5	1.4×10^{-2}	8.20×10^{-2}	1.30×10^{-2}	7.59×10^{-2}
2.9×10^5	4.4×10^{-2}	8.20×10^{-2}	4.90×10^{-2}	9.03×10^{-3}
6.9×10^5	1.6×10^{-1}	8.20×10^{-2}	3.21×10^{-3}	1.59×10^{-3}
10^6	2.87×10^{-1}	8.20×10^{-2}	2.66×10^{-3}	7.59×10^{-4}
1.5×10^6	5.87×10^{-1}	8.20×10^{-2}	2.42×10^{-3}	3.37×10^{-4}
2.5×10^6	2.84	8.20×10^{-2}	4.21×10^{-3}	1.21×10^{-4}
5×10^6	1.82×10^1	3.18×10^{-1}	6.74×10^{-3}	1.18×10^{-4}
10^7	6.11×10^1	9.90×10^{-1}	5.66×10^{-3}	9.17×10^{-5}

V. Concluding Remarks

Numerical study of turbulent flow in rotor–stator systems is a difficult problem, both for the numerical procedure and for the turbulence modeling. The numerical difficulties arise mainly from the destabilizing effect of the rotation due to the Coriolis terms on the numerical algorithm. These problems have been overcome by the use of a semi-implicit treatment of the Coriolis force and of a point implicit treatment for the Reynolds stress equations. Thus, we have obtained results for Reynolds numbers up to 10^7 that correspond to the actual rotational speed in turbomachinery. As far as turbulence modeling is concerned, the confinement, the effect of the rotation on the turbulent field, and the possible coexistence of laminar and turbulent regions make it a difficult challenge. As a first approach, our aim was to test the most commonly used models that have become a standard. We have obtained encouraging results with these standard models. The benefits of a second-order modeling appeared clearly for both the mean and the turbulent field. Our results tend to prove that the second-order models are a necessary level of closure for studying turbulent flow in rotor–stator systems. One major discrepancy between the computed and the measured mean velocity profiles is due to the failure of the models to predict the transition. Thus, the inferior prediction of the boundary-layer profile on the stator side by the k–ε model is a result of the failure to capture the laminar to turbulent transition. This is clearly indicated by the vanishing turbulent kinetic energy prediction shown in Fig. 5. We note that the transition is very sensitive to the precise formulation of the low Reynolds number modifications in the coefficients of the model, and so the result obtained is only valid for the particular models considered, which are standard ones. The main capabilities of the RSM model over simple k–ε models is in the modeling of rotation effects. Indeed, the RSM transport model embodies important features that are crucial to model rotation effects. For the second test case, at higher Reynolds numbers where the flow is less sensitive to the transition, the RSM model give a general improvement of the predictions, in particular for the prediction of the Ekman layers. To improve the numerical predictions, our future work will be oriented toward the use of a more general turbulence model as well as taking into account the implicit effects of the rotation on the turbulent field in a simplified way.

Acknowledgments

The computations were carried out on the Cray Y-MP 2E computer of the Institut Méditerranéen de Technologie and on the Cray C98 of the IDRIS, Paris with support of DRET (Group 6) and SNECMA (YKL group). They are here gratefully acknowledged.

References

[1]Daily, J. W., and Nece, R. E., "Chamber Dimension Effects on Induced Flow and Frictional Resistance of Enclosed Rotating Disks," *Journal of Basic Engineering*, Vol. 82, March 1960, pp. 217–232.

[2]Daily, J. W., Ernst, W. D., and Asbedian, V. V., "Enclosed Rotating Disks with Superposed Throughflow: Mean Steady and Periodic Unsteady Characteristics of Induced Flow," Hydrodynamics Lab., Massachusetts Inst. of Technology, Rept. 64, Cambridge, MA, April 1964.

[3]Itoh, M., Yamada, Y., Imao, S., and Gonda, M., "Experiments on Turbulent Flow due to an Enclosed Rotating Disk," *Engineering Turbulence Modeling and Experiments*, edited by W. Rodi and E. N. Ganic, Elsevier, New York, 1990, pp. 659–668.

[4]Morse, A. P., "Numerical Prediction of Turbulent Flow in Rotating Cavities," Gas Turbine Conf. and Exhibition, ASME Paper 87-GT-74, Anaheim, CA, June 1987.

[5]Chew, J. W., and Vaughan, C. M., "Numerical Predictions of Flow Induced by an Enclosed Rotating Disk," 33rd Gas Turbine and Aeroengine Congress, ASME Paper 88-GT-127, Amsterdam, 1988.

[6]Iacovides, H., and Theofanopoulos, I. P., "Turbulence Modeling of Axisymmetric Flow Inside Rotating Cavities," *International Journal of Heat and Fluid Flow*, Vol. 12, No. 1, 1991, pp. 2–11.

[7]Wilson, M., Kilic, M., and Owen, J. M., "Computation of Flow in Rotating Disk Systems," Int. Centre for Heat and Mass Transfer, International Symposium on Heat Transfer in Turbomachinery, Athens, Aug. 1992.

[8]Iacovides, H., and Toumpanakis, P., "Turbulence Modeling of Flow in Axisymmetric Rotor–Stator Systems," Proceedings for the 5th International Symposium on Refined Flow Modeling and Turbulence Measurements, Presses de l'Ecole Nationale des Ponts et Chaussies, Paris, Sept. 7–10, 1993.

[9]Yap, C., "Turbulent Heat Momentum Transfer in Recirculating and Impinging Flows," Ph.D. Thesis, Dept. of Mech. Engng, Univ. of Manchester, Manchester, England, UK, Feb. 1987.

[10]Owen, J. M., "Fluid Flow and Heat Transfer in Rotating Disk Systems," 14th International Centre for Heat and Mass Transfer, Symposium on Heat and Mass Transfer in Rotating Machinery, Dubrovnick, Yugoslavia, Sept. 1982.

[11]Owen, J. W., and Rogers, R. H., "Heat Transfer in Rotating Disk Systems," *Rotor–Stator Systems*, Vol. 1, Chapters 6 & 7, edited by W. D. Morris, Wiley, New York, 1989.

[12]Patel, V. C., Rodi, W., and Scheuerer, G., "Turbulence Models for Near Wall Low Reynolds Number Flows: a Review," *AIAA Journal*, Vol. 23, No. 9, 1985, pp. 1308–1319.

[13]Schiestel, R., "Modélisation et simulation des écoulements turbulents," *Traité des Nouvelles Technologies*, Chapter 6, Editions Hermés, Paris, 1993.

[14]Jones, W. P., and Launder, B. E., "The Prediction of Laminarization with a Two-Equations Model of Turbulence," *International Journal of Heat and Mass Transfer*, Vol. 15, Feb. 1972, pp. 301–314.

[15]Launder, B. E., and Sharma, B. I., "Application of the Energy-Dissipation Model of Turbulence to the Calculation of the Flow near a Spinning Disk," *Letters in Heat and Mass Transfer*, Vol. 1, No. 2, 1974, pp. 131–138.

[16]Launder, B. E., Reece, G. J., and Rodi, W., "Progress in the Development of a Reynolds Stress Turbulence Closure," *Journal of Fluid Mechanics*, Vol. 68, No. 3, 1975, pp. 275–285.

[17]Schiestel, R., Elena, L., and Rezoug, T., "Numerical Modeling of Turbulent Flow and Heat Transfer in Rotating Cavities," *Numerical Heat Transfer*, Pt. A., Vol. 24, No. 1, 1993, pp. 45–65.

[18]Fu, S., Launder, B. E., and Leschziner, M. A., "Modeling Strongly Swirling Recirculating Jet Flows with Reynolds Stress Transport Closure," International Symposium of Turbulent Shear Flows, Session 17, Sept. 7–9, Toulouse, France, 1987.

[19]Gibson, M., and Launder, B. E., "Ground Effects on Pressure Fluctuations in the Atmospheric Boundary layer," *Journal of Fluid Mechanics*, Vol. 86, Pt. 3, 1978, pp. 491–511.

[20]Hanjalic, K., and Launder, B. E., "A Reynolds Stress Model of Turbulence and its Application in Thin Shear Flow," *Journal of Fluid Mechanics*, Vol. 52, Pt. 4, 1972, p. 609.

[21]Daly, B. J., and Harlow, F. H., "Transport Equation of Turbulence," *Physics of Fluids*, Vol. 23, No. 11, 1970, pp. 2634–2649.

[22]Patankar, S. V., *Numerical Heat Transfer and Fluid Flow*, Chapters 5 & 6, McGraw-Hill, New York, 1980.

[23]Huang, P. G., and Leschziner, M. A., "Stabilization of Recirculating Flow Computations Performed with Second Moments Closures and Third Order Discretization," 6th International Symposium on Turbulent Shear Flow, Session 20, Cornell Univ., Ithaca, NY, Aug. 7–9, 1985.

[24]Batchelor, G. K., *An Introduction to Fluid Dynamics*, Cambridge Univ. Press, New York, 1967, pp. 195–200.